Inorganic Chemistry

Article

pubs.acs.org/IC

Structural Transition at 360 K in the $CaFe_5O_7$ Ferrite: Toward a New Charge Ordering Distribution

C. Delacotte,[†] F. Hüe,[‡] Y. Bréard,[†] S. Hébert,[†] O. Pérez,[†] V. Caignaert,[†] J. M. Greneche,[§] and D. Pelloquin*,[†]

[†]Laboratoire CRISMAT ENSICAEN UMR CNRS 6508, 6 Boulevard du Maréchal Juin, 14050 Caen Cedex 04, France

[‡]Laboratoire GPM UMR 6634 CNRS, Avenue de l'Université, BP12 76801 Saint Etienne du Rouvray, France

[§]Laboratoire IMMM UMR 6283 CNRS, Avenue Olivier Messiaen, 72085 Le Mans, France

ABSTRACT: An efficient synthesis route is proposed to obtain single phase powder ceramic of $CaFe_5O_7$. This complex structure can be described as an intergrowth between one $CaFe_2O_4$ unit and n = 3 slices of FeO Wüstite-type structure. A detailed structural study has been carried out at room temperature combining transmission electron microscopy (TEM) observations (ED, HREM), scanning transmission electron microscopy (STEM-HAADF), and X-ray diffraction data. The analysis of these data has revealed an unexpected supercell with a monoclinic symmetry. From the *hkl* conditions deduced from the electron diffraction study and the analysis of X-ray diffraction data by simulated annealing, a structural model considering the centrosymmetric $P2_1/m$ setting can be proposed. In addition the first magnetic and electrical transport measurements are reported showing a sharp peak in magnetic susceptibility and a strong localization around 360 K, associated to a structural change from monoclinic setting to orthorhombic one.

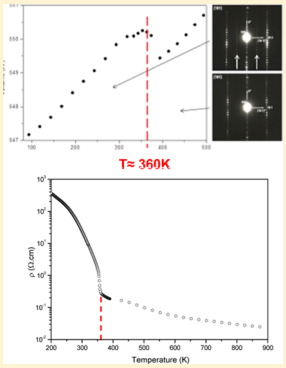

INTRODUCTION

Numerous studies are devoted to mixed valence state iron oxides in materials research due to their complex magnetotransport properties like the famous Verwey transition.[1,2] Among these oxides, special attention during the past decades has been focused on the orthoferrites $LnFeO_3$ (Ln = rare earth) related to the distorted $GdFeO_3$-type perovskite structure which can exhibit some possible spin reorientation transitions versus temperature depending on the nature of Ln.[3−6] Recently, iron based oxides like $LnFe_2O_4$ or perovskite $BiFeO_{3-\delta}$ have also received large attention due to their ability to exhibit some multiferroic properties.[7−9] In these systems, two kinds of Fe species (Fe^{2+} and Fe^{3+}) coexist with localized magnetic moments exhibiting a ferrimagnetic ordering associated to ferroelectric properties. An exciting challenge is to evidence similar properties in other iron based systems. The Ca−Fe−O system offers several interesting candidates, like the $CaFe_5O_7$ phase in regard to the richness of its phase diagram.[10] Except for the $Ca_2Fe_2O_5$ brownmillerite and $CaFe_2O_4$ derived structures, very few microstructural descriptions and physical properties of this system are found in the literature. The first report of the $CaFe_5O_7$ structure,[10] deduced from single crystal data, describes it as an orthorhombic framework built from mixed edge and top shared FeO_6 octahedra filled with Ca columns, with these being spaced by a block of edge shared FeO_6 octahedra. Paradoxically, the magnetotransport properties of this iron rich $CaFe_5O_7$ ferrite have never been analyzed in detail. Nevertheless this material should be promising since, as well as the mixed valence state for the iron species, it exhibits a clear structural relationship with the $CaFe_2O_4$ structure since it can be also described as an intergrowth between a $CaFe_2O_4$ unit and n = 3 slices of FeO Wüstite-type structure.[10]

The major issue with this system lies in its difficulty to grow large single crystals or to isolate monophasic bulk ceramic. In this Article, an efficient synthesis route is proposed to obtain single powder $CaFe_5O_7$ ceramics. A detailed structural study has been carried out combining transmission electron microscopy (TEM) observations (ED, HREM), scanning transmission electron microscopy (STEM-HAADF), and X-ray diffraction data versus temperature. A recent analysis of electron data collected at room temperature[11] has revealed an actual lower monoclinic symmetry associated to some twinning phenomena. In addition the first magnetic and electrical transport measurements are reported in this Article and discussed with respect to the structural features deduced from the current atomic scale observations, *ab initio* structural determination, and Rietveld refinements of actual model. Finally, the structural evolution of the $CaFe_5O_7$ ferrite versus the temperature is shown and correlated to its magnetotransport properties.

EXPERIMENTAL SECTION

The $CaFe_5O_7$ sample was synthesized by a standard solid state reaction process using CaO, Fe_2O_3, and Fe as starting materials in 1:2:1 ratios. The powders were mixed, ground, and uniaxially pressed at about 3 tons/cm^2 into bars (10 × 2 × 2 mm^3). Then, the bars were put into an alumina crucible and sealed under vacuum in a silica tube. The tube was heated for 24 h at 1100 °C in a tubular furnace. The sample was then reground and refired under vacuum at 900 °C for 24 h.

Received: May 20, 2014
Published: September 9, 2014

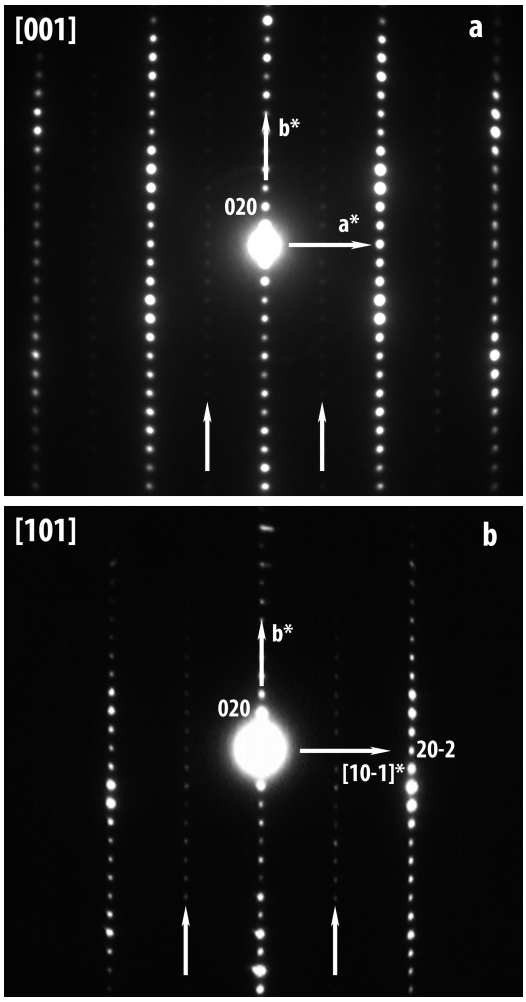

Figure 1. Electron diffraction patterns of (a) [001] and (b) [101] zone axes.

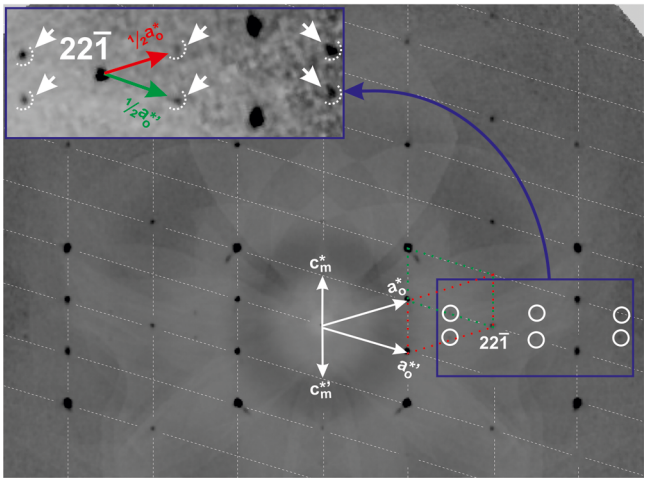

Figure 2. ($h2l$) diffraction plane rebuilt from the frames collected using the single crystal diffractometer. The monoclinic cell $a_m/2$, b_m, c_m is drawn, and some additional peaks leading to the a_m parameters are outlined using white circles.

This last thermal cycle has been repeated to obtain as prepared pure bulk material. Note that single crystals have been also grown according to the method previously reported.[10] Powder X-ray diffraction data were collected using an XpertPro Panalytical diffractometer working

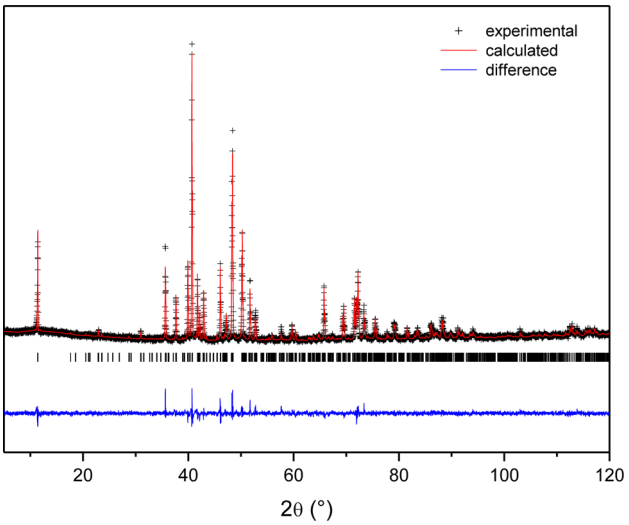

Figure 3. Rietveld refinement of PXRD pattern at RT.

Table 1. Crystallographic Parameters of $CaFe_5O_7$[a]

atom	ox.	Wyckoff	x/a	y/b	z/c	B_{eq}
Ca1	2	2e	0.919(2)	1/4	0.580(3)	0.601
Ca2	2	2e	0.397(3)	1/4	0.595(3)	0.297
Fe1	2	4f	0.161(1)	0.4280(4)	0.566(1)	0.199
Fe2	3	4f	0.236(2)	0.6545(1)	0.9311(6)	0.269
Fe3	2	2a	0	1/2	0	0.427
Fe4	2	4f	0.611(1)	0.4234(4)	0.556(2)	1.251
Fe5	3	4f	0.730(2)	0.6545(1)	0.9311(6)	1.711
Fe6	2	2b	1/2	1/2	0	0.364
O1	−2	2e	0.215(7)	1/4	0.914(3)	0.5
O2	−2	4f	0.979(4)	0.113(1)	0.807(4)	0.5
O3	−2	4f	0.836(4)	0.039(1)	0.328(5)	0.5
O4	−2	4f	0.079(5)	0.166(1)	0.340(4)	0.5
O5	−2	2e	0.736(7)	1/4	0.914(3)	0.5
O6	−2	4f	0.460(5)	0.097(1)	0.850(4)	0.5
O7	−2	4f	0.322(4)	0.031(1)	0.277(5)	0.5
O8	−2	4f	0.580(5)	0.175(1)	0.363(4)	0.5

[a] a = 6.09157(3) Å, b = 17.97446(7) Å, c = 5.25061(2) Å, β = 106.99342(36)°. Space group $P2_1/m$. R_{Bragg} = 0.0889, R_{wp} = 0.0958, χ^2 = 2.17.

with the Co Kα radiation and equipped with an X'Celerator detector and Anton Paar TTK450 thermal chamber. Collection was made over an angular range 5° ≤ 2θ ≤ 120° (step = 0.0167). Lattice constants and the space group were deduced from the electron diffraction (ED) study carried out with a JEOL 2010CX microscope by tilting around crystallographic axes. The high resolution electron microscopy (HREM) was performed with a TECNAI G^2 UT operating at 300 kV (point resolution 1.7 Å, C_S = 0.7 mm). Both microscopes are equipped with EDS (energy dispersive spectroscopy) analyzer. The simulated HREM images have been calculated with the JEMS software. The HAADF images were recorded with a corrected probe JEOL ARM-200 operating at 200 kV and equipped with ADF (annular dark field) detector.

Assuming the cation Ca/Fe ratio deduced from EDS measurements, oxygen content was estimated by picnometry. The *ab initio* structural determination by the simulated annealing method was carried out with the Endeveour software. For the final step, the structural models were refined by the Rietveld method using the software FULLPROF included in the WINPLOTR package[12] and completed by a structural analysis from single crystal diffraction data. A typical platelet-like (50 × 30 × 10 μm^3) single crystal has been extracted, and the corresponding diffraction data were collected on a Nonius Kappa diffractometer

dx.doi.org/10.1021/ic5011456 | Inorg. Chem. 2014, 53, 10171−10177

Table 2. Interatomic Distances (Å)

Ca1−O1	2.12(3)	Ca2−O1	2.26(4)	Fe1−O2	2.05(3)
Ca1−O2	2.71(2)	Ca2−O4	2.51(3)	Fe1−O3	2.06(2)
Ca1−O2	2.71(2)	Ca2−O4	2.51(3)	Fe1−O3	2.10(2)
Ca1−O4	2.35(3)	Ca2−O5	2.25(3)	Fe1−O4	2.05(2)
Ca1−O4	2.35(3)	Ca2−O6	3.03(2)	Fe1−O6	2.04(2)
Ca1−O5	2.34(4)	Ca2−O6	3.03(2)	Fe1−O7	2.16(3)
Ca1−O8	2.45(3)	Ca2−O8	2.31(3)	Fe4−O2	2.34(2)
Ca1−O8	2.45(3)	Ca2−O8	2.31(3)	Fe4−O3	2.18(3)
Fe2−O2	2.28(2)	Fe3−O2	2.26(2)	Fe4−O6	2.05(3)
Fe2−O3	2.46(2)	Fe3−O2	2.26(2)	Fe4−O7	2.12(2)
Fe2−O4	2.04(2)	Fe3−O3	2.33(3)	Fe4−O7	2.10(2)
Fe2−O5	1.89(1)	Fe3−O3	2.33(3)	Fe4−O8	2.02(2)
Fe2−O6	2.14(2)	Fe3−O7	2.15(2)	Ca1−Ca2	3.20(2)
Fe2−O8	2.19(3)	Fe3−O7	2.15(2)	Ca1−Ca2	2.89(2)
Fe5−O1	1.89(1)	Fe6−O3	2.36(2)	Fe1−Fe3	3.02(1)
Fe5−O2	2.04(2)	Fe6−O3	2.36(2)	Fe1−Fe5	3.24(1)
Fe5−O4	2.10(3)	Fe6−O6	1.90(2)	Fe2−Fe4	3.28(1)
Fe5−O6	2.12(3)	Fe6−O6	1.90(2)	Fe3−Fe4	3.12(7)
Fe5−O7	2.44(2)	Fe6−O7	2.13(3)		
Fe5−O8	2.09(2)	Fe6−O7	2.13(3)		

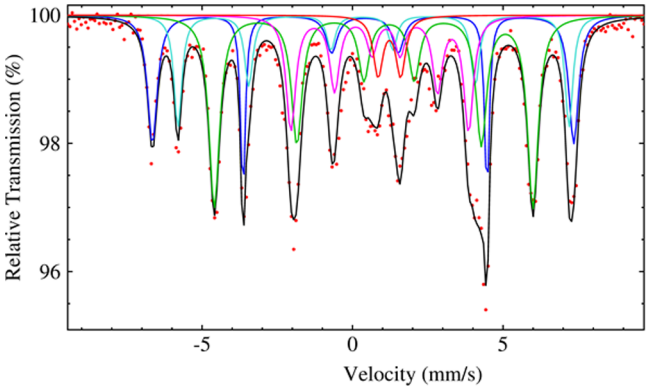

Figure 4. Mossbaüer spectrum of $CaFe_5O_7$ at RT is fitted using 4 sextets and 1 doublet: blue and turquoise sextuplets are Fe^{3+} (with, respectively, IS = 0.38 and 0.50 mm/s), pink is Fe^{2+} (with IS = 1.01 mm/s), green is $Fe^{2+\varepsilon}$ (with IS = 0.96 mm/s). The red doublet is identified with FeO detected as extended defect in the matrix.

(Bruker Nonius) equipped with 2D CCD (coupled charge device) detector using Mo Kα radiation. The data collection was then defined as follows: a D_x (detector−sample distance) value of 34 mm was chosen; Φ- and Ω-scans were used; each frame is measured for a scanning angle of 0.8°. To collect a great number of weak reflections, without saturation by reflections of strong intensity, two different exposure times (45 s/deg and 5 s/deg) were used to collect the data.

The Mossbaüer resonance spectrum was measured at room temperature in transmission geometry using a constant acceleration spectrometer and a ^{57}Co source diffused into a rhodium matrix. The velocity scale was calibrated with a α-Fe foil at room temperature. Isomer shifts (IS) are given relative to α-Fe at room temperature.

Finally, the transport properties (four-probes method) were investigated by means of a physical property measurement system (PPMS) while susceptibility and magnetization were measured from a dc SQUID Quantum Design magnetometer.

RESULTS

Structural Features. According to the experimental conditions described above, a black ceramic is obtained. The preliminary phase analysis from corresponding X-ray power diffraction data (PXRD) collected at room temperature and PDF data bank

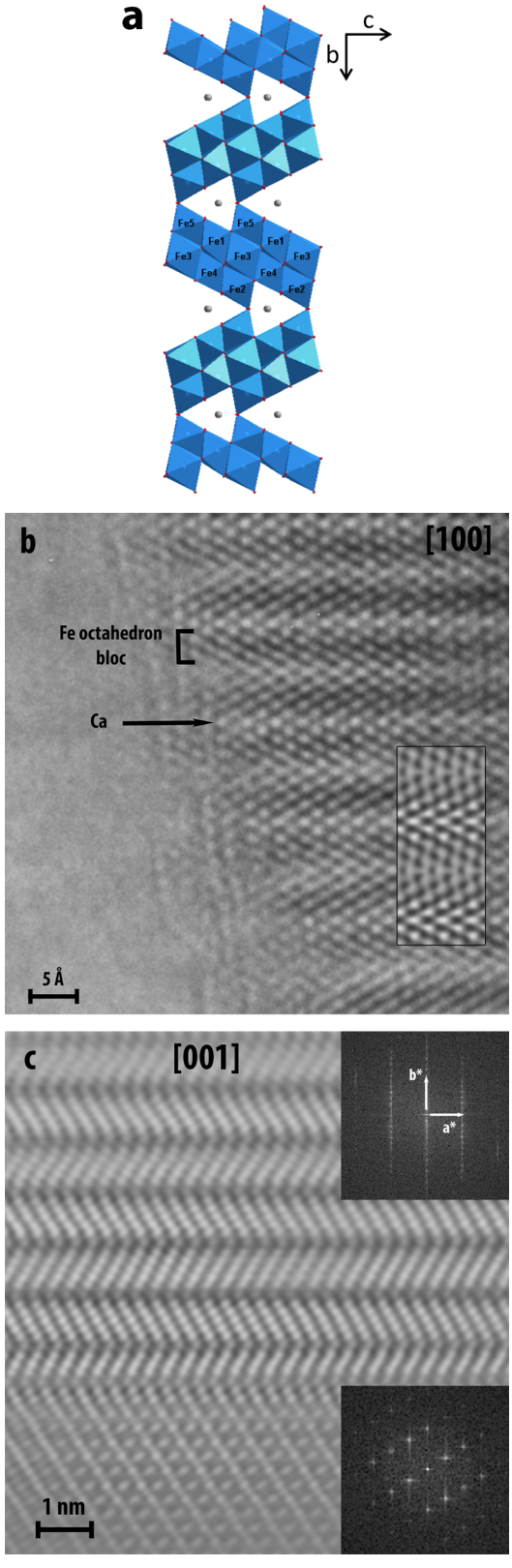

Figure 5. (a) Crystal structure, (b) experimental [100] HREM image collected with a defocus close to −5 nm and thickness from 4 to 6 nm, (c) experimental [001] HAADF with defects along the stacking sequence.

data has confirmed the formation of the expected iron rich $CaFe_5O_7$ phase as main phase. Nevertheless, a recent study at room temperature[11] by means of TEM (transmission electron microscopy) techniques has revealed a more complex lattice

dx.doi.org/10.1021/ic5011456 | Inorg. Chem. 2014, 53, 10171−10177

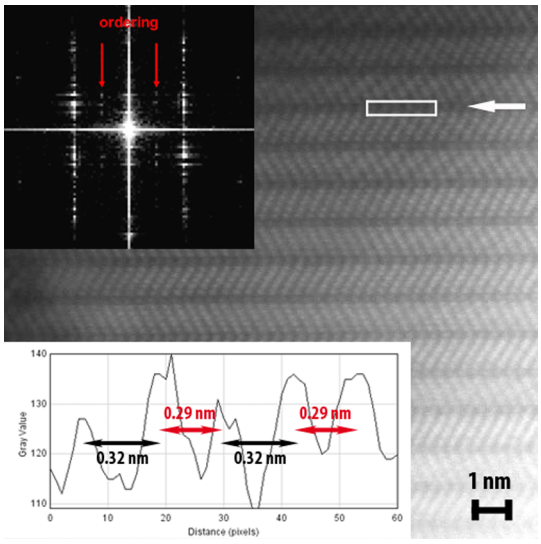

Figure 6. [101] HAADF image and corresponding FFT. Line profile correlated with Ca rows (white rectangle).

compared to the orthorhombic one (a_o =3.05 Å, b_o = 10.05 Å, and c_o = 18 Å) first reported[10] with the existence of fine extra dots. Thus, a monoclinic supercell is found by tilting along the larger cell parameter (Figure 1).

This monoclinic cell exhibits close relationships with the previous one according to the following metric: $a_m = 2a_o$, $b_m = c_o$, $c_m = b_o/2 \sin \beta$, and $\beta = 107°$. Taking into account the single extinction condition, $0k0$ $k = 2n$, the whole X-ray diffraction pattern, especially the splitting of a part of diffraction peaks, can be indexed with the $P2_1$ or $P2_1/m$ space groups and the corresponding refined cell parameters a = 6.0916(1) Å, b = 17.9745(1) Å, c = 5.2506 (1) Å, β = 106.993(4)°. Some very weak reflections inducing the a_o doubling can also be observed on the single crystal X-ray diffraction data but only with a long time exposure (Figure 2). Nevertheless their intensities are too poorly defined to be integrated because of the too small size of single crystals. Note that this work provides evidence also for some twin planes along c^* (red and green cells in Figure 2) as suggested by the ED study.[11] The experimental density deduced from helium picnometry measurements has given ρ_{exp} = 5.22 g/cm^3 in good agreement with the ρ_{calc} = 5.21 g/cm^3 assuming Z = 4, the stoichiometric $CaFe_5O_7$ formula (M = 431.71g), and this actual monoclinic cell. Starting from this analytic result and the powder X-ray diffraction data collected at room temperature, the structural determination by simulated annealing has been considered assuming the monoclinic $P2_1/m$ supercell. This work has allowed us to build a structural model which has been later ratified by some complementary Rietveld refinements. Attempts to work with the lower symmetric $P2_1$ space group have led to similar reliability factors, but some unrealistic distances with large standard deviations are obtained. The final experimental, calculated, and difference plots corresponding to $P2_1/m$ model shown in Figure 3 lead to the R_{Bragg} = 0.0889 and R_{wp} = 0.0958 factors, considering anisotropic atomic displacements for cations and assuming fixed atomic displacements for oxygen atoms. Main corresponding atomic positions and distances deduced from final refinements are summarized in Tables 1 and 2, respectively.

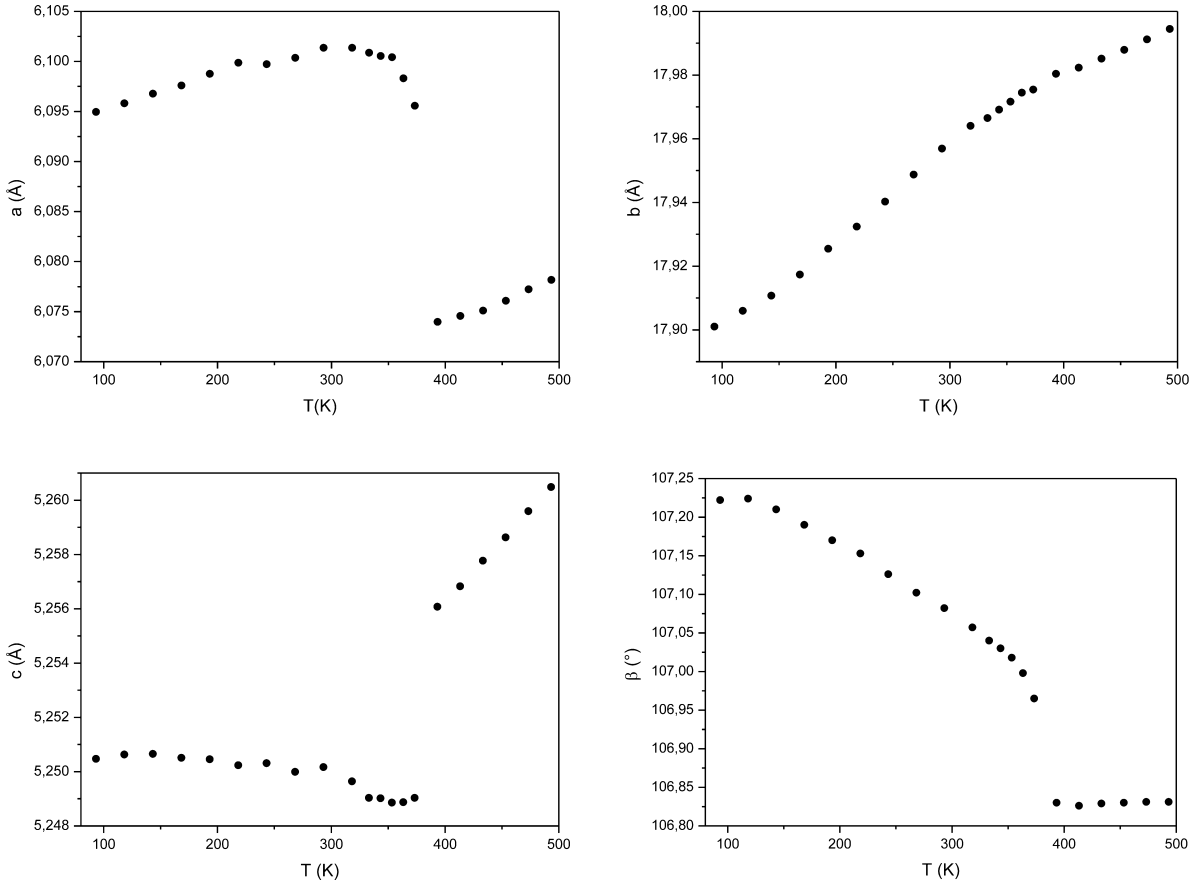

Figure 7. Thermal dependence of monoclinic cell parameters.

dx.doi.org/10.1021/ic5011456 | Inorg. Chem. 2014, 53, 10171−10177

These calculations lead to a structural model (Figure 5a) close to the one previously reported[10] except for the shifting of calcium positions inside the channels along the *c* axis leading to two specific Ca−Ca bonds along *a* axis, 2.89 and 3.20 Å, respectively (Table 2). From this structural model (Figure 5a), six independent iron positions are found, and the analysis of their coordination polyhedral provides evidence for more or less distorted octahedra with some Fe−O distances ranging from 1.89 to 2.46 Å. Even if their individual description must be made cautiously, the oxygen environment of both Fe2 and Fe5 forming channels in which Ca rows are running exhibits one shorter distance close to 1.89 Å corresponding to the shared top oxygen. Consequently the position of these iron species is shifted from the octahedral barycenter. The four other iron sites exhibit more regular octahedral coordinations with distances ranging from 1.90 to 2.36 Å and share an edge to form zigzag chains along the *c* axis (Figure 5a). Taking into account the chemical formula $CaFe_5O_7$, the iron species average valence state is +2.4 and implies the coexistence of Fe^{3+} and Fe^{2+}. This coexistence of several valence states and/or electronic configurations for iron species is exemplified by the Mossbaüer spectrum recorded at RT and shown in Figure 4. The spectrum can be fitted with at least four sextets with isomer shift (IS) ranging from 0.38 to 1.01 mm/s. Two sextets with the lowest IS (IS = 0.38 and 0.50 mm/s) are assigned to Fe^{3+} in octahedral coordination[13] while the sextet with the highest IS (1.01 mm/s) is assigned to Fe^{2+} in octahedral coordination.[13] The fourth sextet, with IS = 0.96 mm/s, suggests that there are still intermediate charge states $Fe^{2+\varepsilon}$ in $CaFe_5O_7$ at RT. According to these structural features and the multiplicity of iron positions (Table 1), the Fe^{3+} species could be mainly located on the Fe2 and Fe5 sites, i.e., at the level of $CaFe_2O_4$ block. Nevertheless a neutron diffraction study will be necessary to determine oxygen atomic displacements properly and confirm this distribution also suggested by the single crystal analysis.[10] In order to complete this structural analysis, HREM images have been recorded along the main zone axes and compared with the corresponding simulated images. Like the experimental [100] oriented HREM image shown in Figure 5b, the simulation fits well the experimental one. Note that some extended defects due to the possible presence of extra [FeO] layers are often observed along the stacking sequence as illustrated by the HAADF image shown in Figure 5c. These defects are identified as the [110] zone axis of $Fe_{0.925}O$ structure.[14] Such orientation leads to a distance $d = 3.079$ Å $\approx a_m/2$ at the interface "defect-stacking sequence". This analysis is in agreement with the EDS measurements focused on these defect zones and highlights the higher Fe/Ca ratio in comparison to the one expected for $CaFe_5O_7$ compound. Such phenomena illustrate the possibility to isolate higher members of the generic series $(CaFe_2O_4)(FeO)_n$.

The superstructure effect is mainly visible on the electron diffraction patterns and tends to disappear after a more or less long irradiation time under the electron beam. This feature can be associated with the sensitivity in temperature detected in this material (see next part concerning thermal dependence). Nevertheless, even if this superstructure is not very stable, its impact can be imaged as illustrated by the HAADF [101] oriented image shown in Figure 6. A complex contrast is observed at the level of iron rows while an alternating dark and gray contrast can be observed between successive light dots related to calcium rows (white arrow in Figure 6). This ordering contrast that reveals two specific distances between successive Ca rows (see profile line in insert) is consistent with

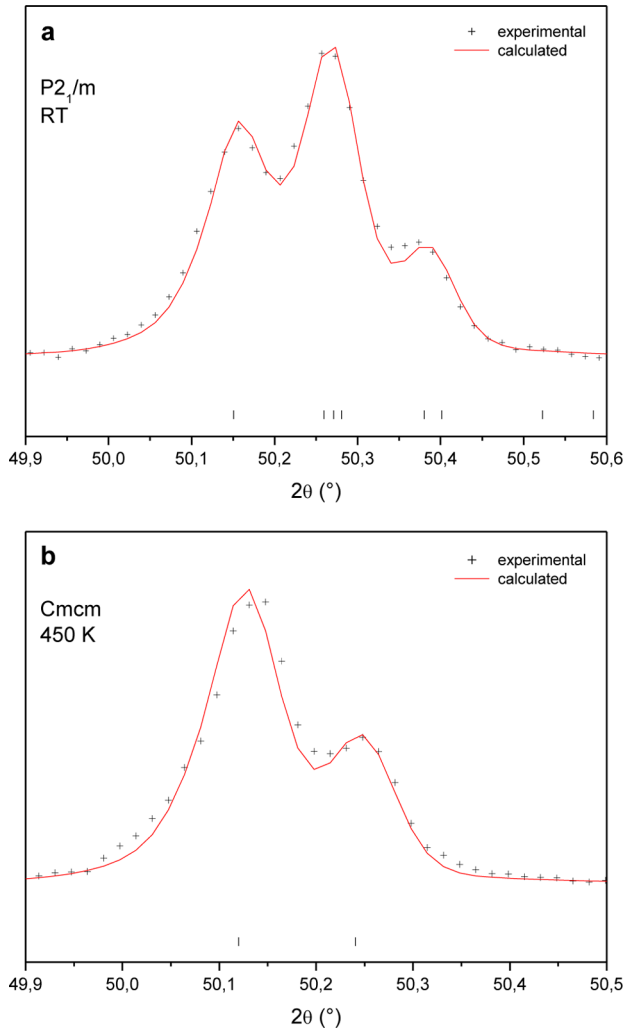

Figure 8. (a) Enlargement of PXRD pattern at RT refined with $P2_1/m$ space group and (b) at 450 K refined with *Cmcm* space group (a_o = 3.04 Å, b_o = 10.08 Å, and c_o = 18.01 Å).

the Rietveld analysis and the Ca−Ca distances that can be deduced (Table 2). The origin of this shift is puzzling, but a tilting of the FeO_6 octahedra forming the calcium channels can be proposed.

Thermal Dependence of the Crystal Structure. To complete this structural analysis, a PXRD study versus temperature was performed from 100 up to 500 K. Figure 7 shows thermal variation of the monoclinic $CaFe_5O_7$ cell parameters (refined using Rietveld method). Three of these parameters (*a*, *c* axes and β angle) exhibit a clear discontinuity around 360 K while the larger cell parameter *b*, related to the stacking sequence, evolves with more regularity. Above this temperature, only the β parameter seems to be stable. The analysis of diffraction peak profile versus temperature shows that some peaks are split on the diffraction patterns recorded below 360 K[11] and becomes single above 360 K (Figure 8).

This observation is consistent with a structural transition from a monoclinic to an orthorhombic cell. The evolution of the unit cell volume confirms this transition at 360 K (Figure 9a). In parallel, an ED study versus temperature was also carried out. Clearly, fine extra dots observed at RT (under 360 K) on electron diffraction patterns have disappeared above 360 K, and the reconstruction of the lattice tilting around main axes leads to an

dx.doi.org/10.1021/ic5011456 | *Inorg. Chem.* 2014, 53, 10171−10177

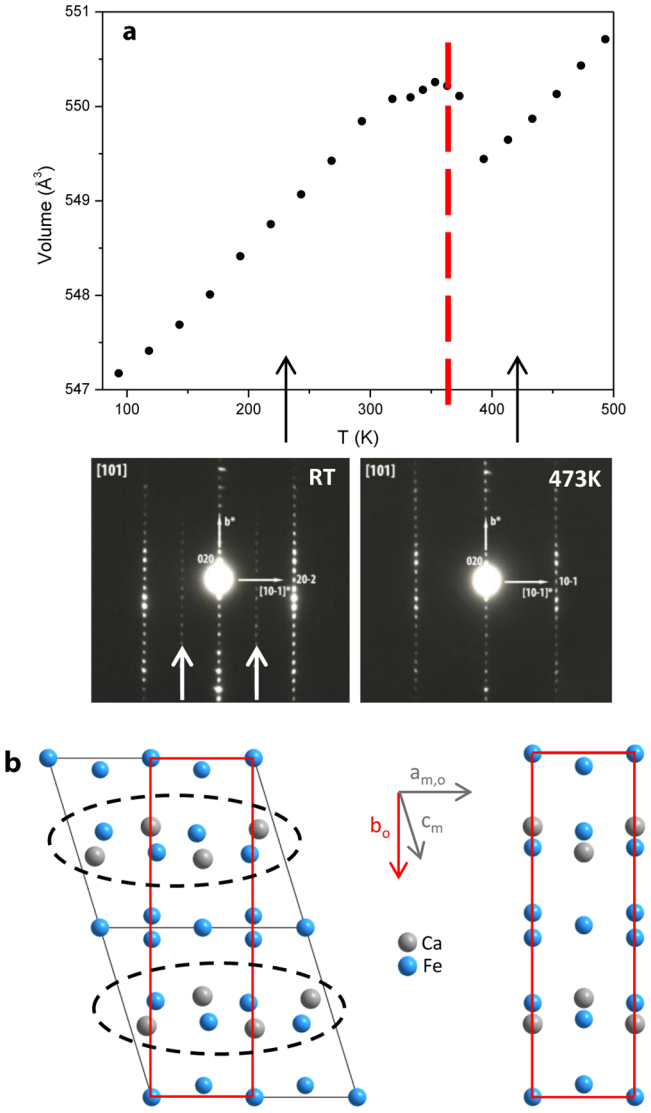

Figure 9. (a) Thermal dependence of monoclinic unit cell volume with corresponding [101] ED zone axis below and above 360 K. (b) Structural projection of monoclinic ([010] zone axis) and orthorhombic ([001] zone axis) forms.

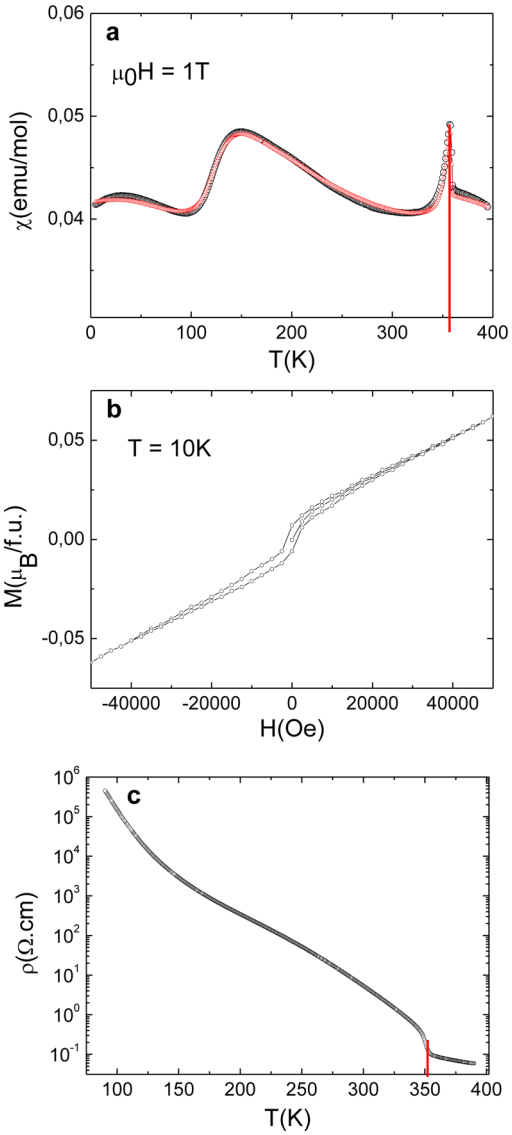

Figure 10. Thermal dependence of (a) magnetic susceptibility in a magnetic field of 1 T (black and red curves are related to zero field cool and field cool, respectively), (b) magnetization loops at 10 K, (c) electrical resistivity.

orthorhombic C-type cell (a_o = 3.05 Å, b_o = 10.05 Å, and c_o = 18 Å) similar to the one first reported.[10] So the "high temperature" structural form obtained at T > 360 K can be related to this orthorhombic structure.

Indeed, the Rietveld refinements starting from this structural model have led to some satisfactory reliability factors as exemplified by Figure 8b and support this scenario. Regarding structural projection (Figure 9b), transition from orthorhombic to monoclinic structure results in a shifting of Ca, Fe1, and Fe4 rows (black dotted circles). Interestingly, if the sample is cooled down to RT after this heating process, the extra dots reappear on electron diffraction patterns. This shows the reversibility of this structural transition and points out that the latter is not due to a change in oxygen stoichiometry. In another way, this structural evolution depending on temperature, especially around 360 K, corroborates the instability of the superstructure under the electron beam during the analysis at atomic scale.

Physical Characterizations. The structural evolution observed both in PXRD and ED studies versus temperature can be directly related to transitions shown by physical characterizations. Figure 10a shows the evolution of magnetic susceptibility (zero field cooling and field cooled warming) as a function of T, recorded under 1 T, up to 400 K, at a sweep rate of 1 K/min. Two transitions are observed, with a maximum of χ at ∼150 K, followed by a sharp peak of χ at the characteristic structural transition temperature of 360 K. The susceptibility values remain very small in the whole T range, and almost constant, and the $M(H)$ loops recorded at low T suggest (Figure 10b) antiferromagnetic or ferrimagnetic behavior. At 10 K, M reaches 0.05 μ_B/formula unit (fu) at 5 T, and the $M(H)$ loop is almost reversible. Note that, at T > 360 K, the $M(H)$ loops present a similar shape, with slightly larger values (0.2 μ_B/fu at 5 T) and a larger coercive field, suggesting that the paramagnetic regime will be reached at $T \gg 400$ K. The temperature dependence of the resistivity clearly indicates a semiconducting behavior of $CaFe_5O_7$ over the range of temperature 90−400 K (Figure 10c).

However, a change up to an order of magnitude in few Kelvin associated with T_s (360 K) is observed. Such a transition, which

dx.doi.org/10.1021/ic5011456 | Inorg. Chem. 2014, 53, 10171−10177

is generally due to a sudden localization of electrons, is clearly correlated with the one which appears in the thermal evolution of the magnetic susceptibility. This is strongly reminiscent of charge ordering phenomena as observed for example in $Pr_{0.5}Ca_{0.5}MnO_3$, between Mn^{3+} and Mn^{4+}.[15]

CONCLUDING REMARKS

This work that deals with the structural evolution of the $CaFe_5O_7$ oxide reveals more complex features as previously reported.[10,11] Interestingly, a structural transition from monoclinic to orthorhombic setting is evidenced at 360 K and associated to an unexpected sharp peak in magnetic susceptibility and a drop in resistivity curve. The interplay between the structure, the electronic transport, and the magnetism is characteristic of a possible charge ordering scenario between Fe^{2+}/Fe^{3+}. Now, as for instance in Fe_3O_4, a change in the charge carrier concentration is expected to follow such a charge ordering.[16] Nevertheless, to base such a mechanism, these magnetic features, and their evolution depending on temperature, need to be analyzed from neutron diffraction data and Mossbaüer spectra in order to identify the distribution of the different valence states for the iron species and their positions in the structure.

AUTHOR INFORMATION

Corresponding Author

*E-mail: denis.pelloquin@ensicaen.fr.

Notes

The authors declare no competing financial interest.

ACKNOWLEDGMENTS

The authors acknowledge the financial support of the French Agence Nationale de la Recherche (ANR), through the program "Investissements d'Avenir" (ANR-10-LABX-09-01), LabEx EMC^3. The authors thank Dr. S. Gascoin for technical support in powder X-ray diffraction data recordings versus temperature.

REFERENCES

(1) Verwey, E. J. W. *Nature* **1939**, *144*, 327.
(2) Garcia, J.; Subias, G. *J. Phys.: Condens. Matter* **2004**, *16*, R145.
(3) Bozorth, R.; Kramer, V.; Remeika, J. *Phys. Rev. Lett.* **1958**, *1*, 3.
(4) Gregory, E.; Remeika, J.; Hagedorn, F. *J. Appl. Phys.* **1968**, *39*, 1369.
(5) Leake, J.; Shirane, G.; Remeika, J. *Solid State Commun.* **1968**, *6*, 15.
(6) Sherwood, R.; Remeika, J.; Williams, H. *J. Appl. Phys.* **1959**, *30*, 217.
(7) Van den Brink, J.; Khomskii, D. I. *J. Phys.: Condens. Matter* **2008**, *20*, 434217.
(8) Wang, J.; Neaton, J. B.; Zheng, H. *Science* **2003**, *299*, 1719.
(9) Lubk, A.; Rossell, M. D.; Seidel, J.; Chu, Y. H.; Ramesh, R.; Hytch, M. J.; Snoeck, E. *Nano Lett.* **2013**, *13*, 1410−1415.
(10) Evrard, O.; Malaman, B.; Jeannot, F.; Courtois, A.; Alebouyeh, H.; Gerardin, R. *J. Solid State Chem.* **1980**, *35*, 112−119.
(11) Delacotte, C.; Hüe, F.; Bréard, Y.; Pelloquin, D. *Key Eng. Mater.* **2014**, *617*, 237−240.
(12) Roisnel, T.; Rodriguez-Carvajal, J. *WinPLOTR: A Windows Tool for Powder Diffraction Patterns Analysis*; Materials Science Forum, Proceedings of the Seventh European Powder Diffraction Conference (EPDIC 7), 2000; pp 118−123.
(13) Mesnil, J. *J. Phys. Chem. Solids* **1985**, *46*, 763−789.
(14) Fjellvag, H.; Gronvold, F.; Stolen, S. *J. Solid State Chem.* **1996**, *124*, 52−57.
(15) Wollan, E. O.; Koehler, W. C. *Phys. Rev.* **1955**, *100*, 545.
(16) Walz, F. *J. Phys.: Condens. Matter* **2002**, *14*, R285−R340.